COBEM 2023 27TH INTERNATIONAL CONGRESS OF MECHANICAL ENGENEERING

ABCM Brazilian Society of Mechanical Sciences and Engineering
27th ABCM International Congress of Mechanical Engineering
December 04-08, 2023, Florianópolis-SC, Brazil

COB-2023-0647
ATTITUDE DETERMINATION AND CONTROL OF A NANOSATELLITE DETECTOR OF COSMIC SOURCES OF X AND GAMMA RAYS

Matheus A. Soares*
Luiz S. Martins-Filho*
Leandro Baroni*
*Universidade Federal do ABC. Av. dos Estados, 5001, 09210-580, Santo André, São Paulo, Brazil.
m.almeida@aluno.ufabc.edu.br, luiz.martins@ufabc.edu.br, leandro.baroni@ufabc.edu.br

Otávio S. C. Durão**
**CRON Sistemas e Tecnologias Ltda. Av. Shishima Hifumi, 2911, 12244-000, Urbanova, Parque Tecnológico UNIVAP, Anexo Escritório 3, São José dos Campos, SP.
otaviodurao@cronsistec.com.br

Valter R. Schad***
***HORUSEYE TECH Engenharia de Sistemas Ltda. Av. Shishima Hifumi, 2911, 12244-000, Urbanova, Parque Tecnológico UNIVAP, Anexo Escritório 1, São José dos Campos, SP.
horuseye@horuseye.com.br

Abstract. *NANOMIRAX is a 2U CubeSat nanosatellite whose payload consists of an experiment to detect and localize hard X-rays/gamma rays from cosmic explosions called "Localizador de Explosões Cósmicas de Raio-X" (LECX – Portuguese for Locator of X-ray Cosmic Explosions), composed by detectors with 53°×53° of a field of view. For this mission purpose, the experiment should not be pointed toward Earth, but rather around the zenith direction of the orbit. The control, using active magnetic actuators, has three modes: detumbling, limit zone and slowdown. The first and third ones aims to decrease the angular velocity of the satellite about a main axis. The second aims to prevent the sensors from being pointed towards the center of the Earth and to maximize the radiation search area. The modeling of the NANOMIRAX orbital and attitude movement was validated in numerical simulations, considering the conditions planned for the mission in terms of orbit, the strategy of attitude determination, and the three modes control to calculate the torques to be produced with magnetorquers. The simulations considered the magnetization and demagnetization cycles for electromagnetic actuation.*

Keywords: *Magnetic attitude control, Attitude determination, Attitude control, B-dot control, CubeSat*

1. INTRODUCTION

The NANOMIRAX/CRON-1 is a nanosatellite designed as a CubeSat platform composed of 2 units (2U) of standard cubes (10 cm×10 cm×10 cm). One cube is dedicated to the operational satellite subsystems and the other to the payload, the experiment "Localizador de Explosões Cósmicas de Raio-X" (LECX – Portuguese for Locator of X-ray Cosmic Bursts). This project is a continuation of the protoMIRAX, an experimental balloon that carried the MIRAX (X-ray Monitor and Imager). The total mass is expected to be 2.1 kg, with 600 g for the payload. The total power is 2.2 W, of which 800 mW is dedicated to the experiment. The LECX is composed of a hard X-ray imaging camera (range 10 to 200 keV) of four CdZnTe (Cadmium, Zinc, Tellurium) detectors with 10 mm ×10 mm×2 mm in the 2×2 arrangement so that the capture area is 400 mm^2. Below 100 keV electromagnetic radiation is dominant over background noise. It is estimated that the experiment will be able to detect approximately 5 gamma-ray bursts (GRBs) per year. There is no need of appointment control in this project but the appointment stability in flight to know the attitude when detecting a cosmic explosion. Furthermore, it is expected that the CubeSat can rotate to increase probability of detection. The Attitude Determination and Control Module (ADCM) consists of a triad of magnetometers, solar sensors on the outer faces of the nanosatellite, a triad of gyroscopes (gyros). The actuators available are three magnetic actuators (magnetorquers), two of which with ferrous core and the third with air core. (Braga et al., 2004) (Braga et al., 2015) (Braga et al., 2020) (Durão et al., 2019).

Since sensors must find gamma rays generated by cosmic explosions, aiming at Earth is a situation that should be avoided if possible. Therefore, in addition to detumbling, a control technique with the objective of avoiding orientations that lead the LECX to face the earth's surface was considered. In the literature we can find attitude control projects for satellites whose payload are x-ray sensors. In Ninomiya *et al.* (1990), a safe-hold control for the Astro-D a satellite is proposed, considering a high-throughput X-ray telescope and the attitude system composed of four small sized momentum

wheels to evaluate a high pointing accuracy. Pirayesh *et al.* (2018) studied an optimization of attitude control of the Virtual Telescope for X-Ray Observations (VTXO), project involved two 6U CubeSat with a PD-Control that maintain the spacecrafts pointed to Crab Nebula. Another interesting mission involving X-Ray Imaging is the Atmospheric Effects of Precipitation through Energetic X-Rays (AEPEX), as described in Berland *et al*. (2021), proposed to study the radiation belt precipitation and radiation belt lifetimes using a 6U CubeSat whose range spectra is 50-300 keV, as near as LECX.

This paper is divided as follows: Section 2 presents the satellite model, the reference frames utilized and attitude kinematics and dynamics with attitude determination. Section 3 presents the attitude control approach considering three different modes. Section 4 presents the numerical simulation results and discussions. Finally, Section 5 concludes the article.

2. SATELLITE MODEL

For the proper analysis of satellite orientation, reference frames should be well-defined. Firstly, the Earth-Centered Inertial Frame (ECI), whose origin is located in the Earth's center of mass, is defined by I, with x-axis pointing to the intersection of the vernal equinox and equatorial plane, z-axis is oriented in the direction of the Geographical North Pole and y-axis completes the right-handed orthogonal system located in the equatorial plane. The Orbital Reference Frame (ORF) has its origin established in the satellite center of mass indicated by O where z-axis aligns to the nadir vector, i.e., the direction toward Earth's center of mass from the satellite, y-axis points to the opposite direction of the normal orbit vector, negative to orbital angular momentum vector and x-axis completes the right-handed triad. This frame is also known as Local-Vertical/Local-Horizontal Frame (LVLH). The ECI and ORF are illustrated in Figure 1, with velocity vector from orbital motion in red. To conclude, the Body Reference Frame (BRF) is fixed on the satellite whose origin is attached to its center of mass. The frame is specified by B, with z-axis pointed to the longitudinal direction of the satellite where the utmost is the opposite direction of the LECX sensor, x-axis lies in the direction of the blue face in Figure 2 (the others are in cyan) and y-axis is orthogonal to the other axes. It is assumed that this frame is coincident with the principal axis, a direction where the moment of inertia matrix is diagonal.

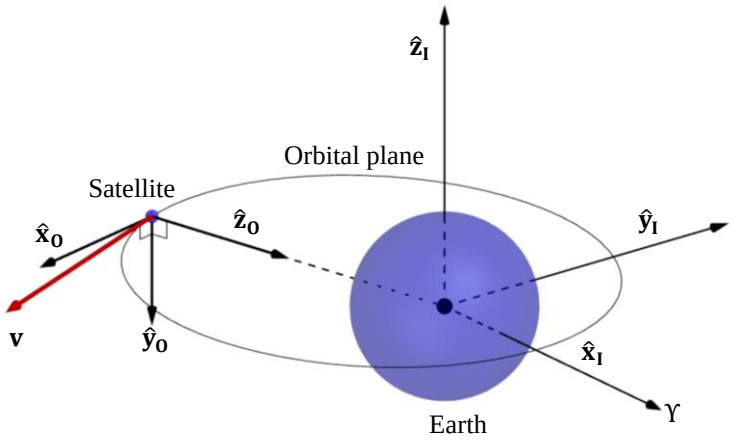

Figure 1. Earth-Centered Inertial Frame (ECI): $\hat{\mathbf{x}}_\mathbf{I}$ (pointing vernal equinox Υ), $\hat{\mathbf{y}}_\mathbf{I}, \hat{\mathbf{z}}_\mathbf{I}$; Orbital Reference Frame (ORF): $\hat{\mathbf{x}}_\mathbf{O}, \hat{\mathbf{y}}_\mathbf{O}, \hat{\mathbf{z}}_\mathbf{O}$ and velocity vector $\mathbf{v}$ (in red).

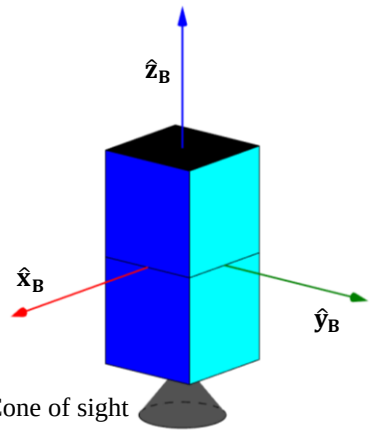

Figure 2. Body Reference Frame (BRF): $\hat{\mathbf{x}}_\mathbf{B}, \hat{\mathbf{y}}_\mathbf{B}, \hat{\mathbf{z}}_\mathbf{B}$ and Cone of sight.

The transformation of a vector expressed in a general frame D to its representation in another frame C corresponds to a multiplication of a proper real orthogonal called rotation matrix, attitude matrix, or direction cosine matrix $\mathbf{A_{CD}}$ with properties $\mathbf{A_{CD}^{-1}} = \mathbf{A_{CD}^{T}} = \mathbf{A_{DC}}$, $\det \mathbf{A_{CD}} = 1$. A rotation from frame ORF to ECI is expressed by $\mathbf{A_{IO}}$, calculated as:

$$\mathbf{A_{IO}} = [\mathbf{o_{1I}} \quad \mathbf{o_{2I}} \quad \mathbf{o_{3I}}] \tag{1}$$

where $\mathbf{o_{1I}}, \mathbf{o_{2I}}$ and $\mathbf{o_{3I}}$ are the representation of the axis from O frame as:

$$\begin{aligned} \mathbf{o_{3I}} &= -\mathbf{r_I}/\|\mathbf{r_I}\| \\ \mathbf{o_{2I}} &= -\mathbf{h_I}/\|\mathbf{h_I}\| = -(\mathbf{r_I} \times \mathbf{v_I})/\|\mathbf{r_I} \times \mathbf{v_I}\| \\ \mathbf{o_{1I}} &= (\mathbf{o_{2I}} \times \mathbf{o_{3I}}) \end{aligned} \tag{2}$$

as $\mathbf{r_I}$ and $\mathbf{v_I}$ represent position and velocity vectors of the spacecraft at a certain instant in the inertial frame. In this work, we treat attitude of the satellite as the orientation of its body frame concerning the orbital frame. Then, to describe this

formulation and its variation in time we implement unit quaternions to parameterize the attitude matrix. A quaternion is a $\mathbf{Q} \in \mathbb{R}^4$ vector defined as $\mathbf{Q} \equiv [q_1 \quad q_2 \quad q_3 \quad q_4]^T = [\mathbf{q}^T \quad q_4]^T$ as $\mathbf{q} = [q_1 \quad q_2 \quad q_3]^T$ is the vector and q_4 is the scalar parts of the quaternion such that it holds $\mathbf{q}^T\mathbf{q} + q_4^2 = 1$. Hence, the direction cosine matrix parameterized by quaternions follows (Markley and Crassidis, 2014) (Wertz, 1978):

$$\mathbf{A}(\mathbf{q}) = (q_4^2 - \|\mathbf{q}\|^2)\mathbf{I_3} - 2q_4[\mathbf{q}\times] + 2\mathbf{q}\mathbf{q}^T \tag{3}$$

where $\mathbf{I_3} \in \mathbb{R}^{3\times3}$ is the identity matrix, $[\mathbf{q}\times]$ is the skew-symmetric matrix of a general $\mathbb{R}^3$ vector defined by:

$$[\mathbf{q}\times] \equiv \begin{bmatrix} 0 & -q_3 & q_2 \\ q_3 & 0 & -q_1 \\ -q_2 & q_1 & 0 \end{bmatrix} \tag{4}$$

Thus, a transformation relating frame B to O is given by matrix $\mathbf{A_{BO}} = \mathbf{A}(\mathbf{q_{BO}})$.

2.1. Attitude kinematics and dynamics

Modelling the spacecraft as a rigid body, the attitude kinematics and dynamics relating are governed by (Wertz, 1978) (Crassidis and Junkins, 2012) (Markley and Crassidis, 2014):

$$\mathbf{q}_{k+1} = \Theta\left(\boldsymbol{\omega}_{\mathbf{B}_k}^{\mathbf{BO}}\right)\mathbf{q}_{\mathbf{BO}_k} \tag{5}$$

$$\boldsymbol{\omega}_{\mathbf{B}}^{\mathbf{BI}}{}_{k+1} = \boldsymbol{\omega}_{\mathbf{B}}^{\mathbf{BI}}{}_{k} + \Delta\boldsymbol{\omega}_{\mathbf{B}}^{\mathbf{BI}}{}_{k}\Delta t \tag{6}$$

where $\boldsymbol{\omega}_{\mathbf{B}}^{\mathbf{BO}}$ is the angular velocity of body frame related to orbit, expressed in B frame and $\boldsymbol{\omega}_{\mathbf{B}}^{\mathbf{BI}}$ is the angular velocity of body frame related to inertial frame, expressed in the same B frame, $\Theta\left(\boldsymbol{\omega}_{\mathbf{B}_k}^{\mathbf{BO}}\right)$ is the propagation function for quaternions defined as:

$$\Theta\left(\boldsymbol{\omega}_{\mathbf{B}_k}^{\mathbf{BO}}\right) = \begin{bmatrix} \cos\left(\left\|\boldsymbol{\omega}_{\mathbf{B}_k}^{\mathbf{BO}}\right\|\Delta T/2\right)\mathbf{I_3} - [\boldsymbol{\psi}_k\times] & \boldsymbol{\psi}_k \\ -\boldsymbol{\psi}_k & \cos\left(\left\|\boldsymbol{\omega}_{\mathbf{B}_k}^{\mathbf{BO}}\right\|\Delta T/2\right) \end{bmatrix} \tag{7}$$

with

$$\boldsymbol{\psi}_k \equiv \frac{\sin\left(\left\|\boldsymbol{\omega}_{\mathbf{B}_k}^{\mathbf{BO}}\right\|\Delta T/2\right)}{\left\|\boldsymbol{\omega}_{\mathbf{B}_k}^{\mathbf{BO}}\right\|}\boldsymbol{\omega}_{\mathbf{B}_k}^{\mathbf{BO}} \tag{8}$$

where ΔT is the kinematics sample interval time and Δt is the dynamics sample interval time which is a hundred times less than ΔT(explanations are given in section 3.3) and $\Delta\boldsymbol{\omega}_{\mathbf{B}}^{\mathbf{BI}}{}_{k}$ is the time derivative of angular velocity vector as:

$$\Delta\boldsymbol{\omega}_{\mathbf{B}}^{\mathbf{BI}}{}_{k} = \boldsymbol{J}^{-1}\left[\boldsymbol{\tau}_c + \boldsymbol{\tau}_{gg} - \left(\boldsymbol{\omega}_{\mathbf{B}}^{\mathbf{BI}}{}_{k} \times \mathbf{J}\boldsymbol{\omega}_{\mathbf{B}}^{\mathbf{BI}}{}_{k}\right)\right] \tag{9}$$

with $\mathbf{J}$ being the inertia matrix, $\boldsymbol{\tau}_c$ the external control torque vector and $\boldsymbol{\tau}_{gg}$ is the gravity gradient torque. Since BRF is chosen with its axes coincident with the principal axes of inertia, thus $\mathbf{J} = \mathrm{diag}(J_x, J_y, J_z)$. The angular velocities are related by rotational motion between inertial and body frame as:

$$\boldsymbol{\omega}_{\mathbf{B}}^{\mathbf{BI}} = \boldsymbol{\omega}_{\mathbf{B}}^{\mathbf{BO}} + \boldsymbol{\omega}_{\mathbf{B}}^{\mathbf{OI}} = \boldsymbol{\omega}_{\mathbf{B}}^{\mathbf{BO}} + \mathbf{A_{BO}}\boldsymbol{\omega}_{\mathbf{O}}^{\mathbf{OI}} \tag{10}$$

where $\boldsymbol{\omega}_{\mathbf{O}}^{\mathbf{OI}} = [0 \quad -\omega_s \quad 0]^T$ is the orbital angular velocity vector in orbital frame due to ω_s is the orbital rate. In this work, the control torque is generate using only magnetic actuators. The resulting control torque is given by:

$$\boldsymbol{\tau}_c = \mathbf{m_B} \times \mathbf{b_B} \tag{11}$$

with $\mathbf{m_B}$ representing the dipole moment generated by the actuators and $\mathbf{b_B}$ is the density of magnetic flux in body frame. The only attitude perturbation considered here is the torque caused by gravity gradient expressed as (Markley and Crassidis, 2014) (Viegas and Waldmann, 2010) (Desouky and Abdelkhalik, 2019):

$$\boldsymbol{\tau}_{gg} = (3\omega_s^2/\|\mathbf{r_O}\|^2)[\mathbf{r_O} \times \mathbf{J}\mathbf{r_O}] \tag{12}$$

2.2. Attitude determination

The calculation of Sun's Position is based on the methods described in Markley and Crassidis (2014: 420-422), Vallado (2013: 277-281), Zheng et al. (2019), extracting the position vector in ECI frame. The geomagnetic field is calculated using IGRF13 (International Geomagnetic Reference Field 13 Model) as described in Alken et al. (2021) and implemented as Davis (2004). To simulate solar sensor and magnetometers measurements, it is necessary to transform sun position and magnetic flux density in BRF, respectively, $\mathbf{b_B}$ and $\mathbf{s_B}$, adding a Gaussian noise as uncertainty. The attitude quaternion relating ORF and BRF, $\mathbf{q_{BO}}$, is determined by a QUEST algorithm where reference direction is formed concatening geomagnetic vector and sun position vector in ORF as $\mathbf{r^q} = [\mathbf{b_O^T} \quad \mathbf{s_O^T}]^T$ and measure direction is $\mathbf{m^q} = [\mathbf{b_B^T} \quad \mathbf{s_B^T}]^T$ (Shuster and Oh, 1981) (Shuster and Natanson, 1993) (Cheng and Shuster, 2014). As the quaternion geometry is hard to be visualized, a 3-2-1 Euler Angles representation is used to express $\mathbf{q_{BO}}$ as three rotations with angles ϕ, θ, ψ (yaw, pitch, and roll angles). The conversion from quaternion to angles is computed using (Markley and Crassidis, 2014) (Wertz, 1978):

$$\begin{aligned} \psi &= \tan^{-1}[2(q_1q_2 + q_4q_3)/(q_1^2 - q_2^2 - q_3^2 + q_4^2)] \\ \theta &= \sin^{-1}[-2(q_1q_3 - q_4q_2)] \\ \phi &= \tan^{-1}[2(q_2q_3 + q_4q_1)/(-q_1^2 - q_2^2 + q_3^2 + q_4^2)] \end{aligned} \tag{13}$$

In eq. (5), $\mathbf{q}_{k+1}$ is not used to determine $\mathbf{q_{BO}}_{k+1}$, instead, it parameterizes the new attitude matrix, i.e., $\mathbf{A_{BO}}_{k+1}$. This procedure propagates the sensor measurements and then QUEST algorithm estimates the new quaternion $\mathbf{q_{BO}}_{k+1}$.

3. ATTITUDE CONTROL

The main mission of NANOMIRAX is to capture and register gamma-rays bursts. It is desirable that angular velocity $\boldsymbol{\omega}_\mathbf{B}^\mathbf{BO}$ be diminished close to zero, but not nullified, since the sensors motion can increase the probability of finding gamma-ray bursts. However, Earth pointing configuration must be avoided because it should generate false data. Consequently, attitude control is required to achieve hierarchic objectives: 1) detumbling, 2) avoid Earth pointing, 3) slowdown angular velocity. These three phases are described as follows.

3.1. Detumbling and Slowdown Modes

After separation from the launch vehicle, the satellite has a large angular momentum not adequate to allow capture of gamma-ray bursts. Detumble consists of reducing the angular velocity varying current induced in magnetorquers such that generate an interaction with local magnetic field alternating control torque. The control law governing this mode is the B-dot law based on:

$$\mathbf{m}_\mathbf{B}^{bdot} = -\frac{k_m}{\|\mathbf{b_B}\|^2}\dot{\mathbf{b}}_\mathbf{B} \tag{14}$$

where $k_m = 2\omega_0 J_{min}$ is the control gain proposed by Avanzini and Giulietti (2012) and $\dot{\mathbf{b}}_\mathbf{B}$ is the rate of change of magnetic flux density. The control gain will be given as 10^{-5} kg.m^2/s (value is showed in section 4) order of magnitude intending to reduce energy consumption that is highly required in satellite missions. It is possible to estimate $\dot{\mathbf{b}}_\mathbf{B}$ as:

$$\dot{\mathbf{b}}_\mathbf{B} \approx \Delta\mathbf{b_B}/\Delta t = \left(\mathbf{b}_{\mathbf{B}_k} - \mathbf{b}_{\mathbf{B}_{k-1}}\right)/\Delta t \tag{15}$$

In the presence of a time varying magnetic field the global asymptotic stability is guaranteed, since $\boldsymbol{\omega}_\mathbf{B}^\mathbf{BO}$ can be reduced to a value near orbit rate (Avanzini and Giulietti, 2012) (Markley and Crassidis, 2014) (Lovera, 2015).

After activating Limit Zone mode, satellite spins faster, then a reduction of angular velocity must be employed. Then, the b-dot control is again utilized. As the detumbling and slowdown modes are basically the same, they must operate in different situations:

1) Detumbling: $\left\|\boldsymbol{\omega}_\mathbf{B}^\mathbf{BO}\right\| > 5°/s$;
2) Slowdown: $\left\|\boldsymbol{\omega}_\mathbf{B}^\mathbf{BO}\right\| \geq 0.5°/s$;

3.2. Limit Zone Mode

A crucial requirement of this mission is the LECX pointing towards space, to capture gamma-ray bursts. The pointing towards Earth configuration must be avoided. Consequently, a control mode needs to be activated in these cases. This mode is called the Limit Zone, and it is employed as a primary condition to generate control torques after detumbling at a certain angular velocity. The LECX camera has a 53° field of view (FoV), and the Earth spheroid cannot be in the

camera cone of sight coming out from under the satellite, in the inverse z-axis direction as defined in the BRF base. Considering that this form is the same height as the satellite's altitude above the earth's surface, then the radius of cone of sight is given by:

$$r_{cs} = h \sin(\alpha_{cs}/2) \tag{16}$$

where h is the altitude of the spacecraft above earth's surface and $\alpha_{cs} = 53°$ is the experiment opening angle. The cone of sight and its location in BRF is represented in Figure 2. The Limit Zone is determined by a cone around the nadir axis of the satellite, i.e., the z-axis of the ORF whose radius is limited by the visualization of the Earth. As simplification, Earth is considered a sphere with Equatorial radius equal to $R_e = 6378137.0$ m. Visualizing Figure 3 it is possible to determine the quantities:

$$s_{lz} = \sqrt{r^2 - R_e^2} \tag{17}$$
$$h_{lz} = s_{lz}^2 / r \tag{18}$$
$$r_{lz} = s_{lz} R_e / r \tag{19}$$
$$\alpha_{lz} = \sin^{-1}(r_{lz}/s_{lz}) = \cos^{-1}(h_{lz}/s_{lz}) \tag{20}$$

where s_{lz} is the slant height, h_{lz} is the height, $r_{lz}$is the radius and α_{lz} is the opening angle of edge zone. As cone of sight is attached with satellite and boundary zone is fixed in ORF, actuators should be activated in limit zone mode when $\delta > 0$, since

$$\delta = 180° - \beta - \alpha_{lz} - \alpha_{cs}/2 \tag{21}$$

where $\beta = \cos^{-1}(\hat{\mathbf{z}}_\mathbf{O} \cdot \hat{\mathbf{z}}_\mathbf{I})$ is the angle between unity vectors in the direction of z-axis of orbital and body frames, respectively. However, applying control close to $\delta \cong 0$ does not prevent the system from spending a period in the boundary zone. Therefore, limit zone control mode must be activated when $\delta \geq \delta_e$ being δ_e a small enough angle. The magnetic dipole moment generated in limit zone mode must be proportional to angular velocity signal as it accelerates the satellite in the opposite direction as it is going, so

$$\mathbf{m}_\mathbf{B}^{lzm} = m_{max} \operatorname{sgn}\left(-\boldsymbol{\omega}_\mathbf{B}^{\mathbf{BO}}\right) \tag{22}$$

where m_{max} is the maximum magnetic moment generated by the torquers. In Figure 4 it is possible to see a representation of cone of sight (black) and limit zone cone (yellow). The cone of sight is smaller than the other, since the edge zone is tangent to the Earth radius. For example, in the situation shown in Figure 4 the limit zone control mode should be activated, as the cone of sight is tending to enter the forbidden zone.

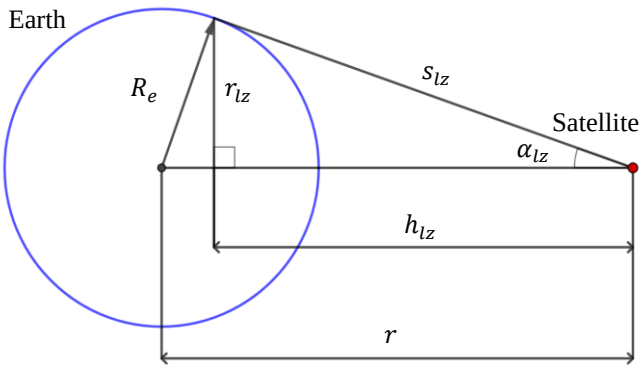

Figure 3. Limit zone trigonometry.

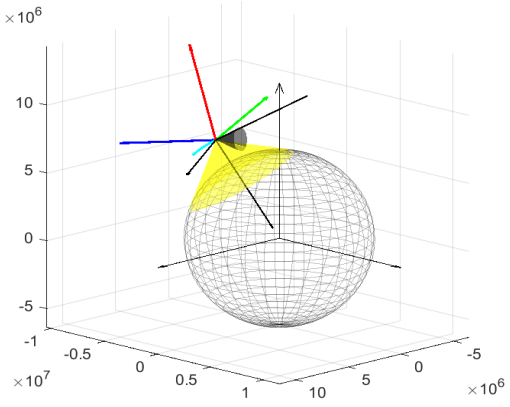

Figure 4. Satellite orbiting Earth: limit zone cone (yellow); satellite cone of sight (black).

3.3. Magnetizing and Demagnetizing Ferromagnets

Generally, the magnetic actuators used in nanosatellites have a ferromagnetic core, to reduce the current required to induce the actuation dipole moment. Nonetheless, intrinsic to ferromagnetic materials are the hysteresis loop. This behavior is not linear and depends on the regressive magnetization history of sample to specify the magnetization state. By exposing a demagnetized ferromagnet to an external magnetic field, it is magnetized in the direction of that field

whose ratio between induced field and magnetic flux density in the sample follows the trajectory of the magnetization curve. This path is followed until saturation, where increasing the magnetic field does not induce magnetization in the material since all magnetic domains are oriented in the direction of the field. As the external field decreases after saturation, the magnetic density does not follow the magnetization curve but a different path so that for a null field there is a residual magnetization or retentivity. To nullify the reminiscence, the magnetic field must be reversed until it reaches the intrinsic coercivity of the material. To demagnetize a ferromagnet, a usual method consists of applying a series of alternating magnetic fields with decreasing amplitude, creating small cycles of hysteresis until the magnetic density is null with null field. This method is called Demagnetizing cycle (Bertotti, 1998) (Cullity and Graham, 2009) (Coey, 2010). An example of hysteresis cycle is illustrated in Figure 5 and demagnetizing cycle in Figure 6.

In the simulation of the behavior of a ferromagnetic actuator, the magnetization curve and the demagnetization cycle were included in this study. Therefore, the time step of updating the sensor data and the actuation must be at different frequencies. Actuators are assumed to operate a hundred times faster than sensors. For now, ΔT is the sample time for kinematics and sensors and Δt is the sample time for actuators and dynamics. 80% of the ΔT must be used to magnetize the ferromagnet until the dipole moment is equal to required and the remaining time must be used to demagnetize the sample. The magnetization of the dipole moment from each rod follows the function (Thornton and Marrion, 2004) (Ogata, 2010):

$$m_{mag}(t) = m\left(1 - e^{-t/k_g}\right) \tag{23}$$

And to demagnetize,

$$m_{dmg}(t) = me^{-\xi t}\cos(\omega_n t) \tag{24}$$

where m is the dipole moment necessary from any control mode, k_g is the growth parameter ξ is the damping parameter and ω_n is the damped oscillator frequency.

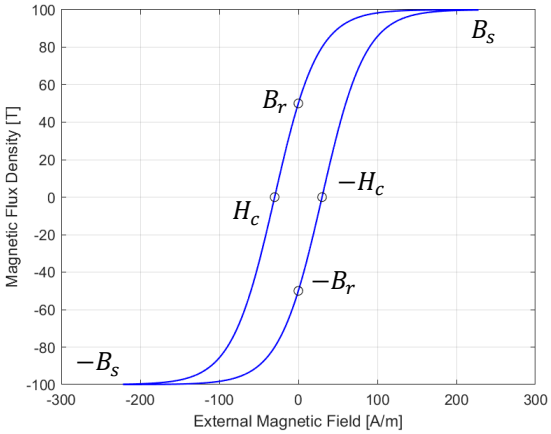

Figure 5. Hysteresis cycle for ferromagnetic material with saturation at $B_s = 100$ T, retentivity $B_r = 50$ T and coercivity $H_c = 30$ A/m.

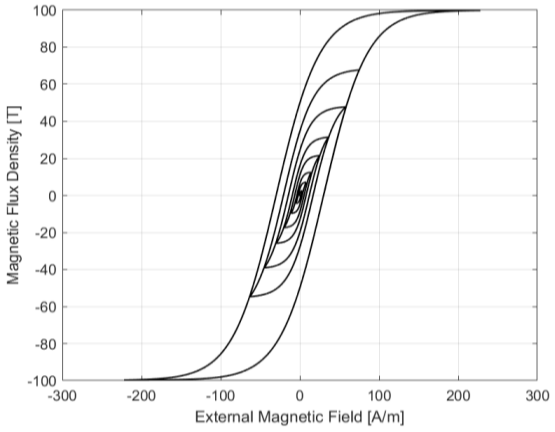

Figure 6. Demagnetizing cycle with decreasing external magnetic field.

4. SIMULATIONS AND RESULTS

The parameters used in the validation simulations are shown in Table 1. As time increases, it is more difficult to visualize the magnetization and demagnetization, given the scale of the graph. Thus, a simulation lasting 5 s was performed to show the details (see Figure 7 and Figure 8). The first one represents the time evolution of dipole moment from actuators in slowdown mode. It is possible to see that the magnetization lasts for 0.10 s and then the actuators maintain the nominal necessary value. After 0.80 s, the beginning of the demagnetization cycle is verified as a damped harmonic oscillator with parameters $\xi = 0.1359$ and $\omega_n = 22.08$ rad/s which varies the magnetization until it is null. The parameters were chosen such that every 10 ms the value of the magnetic field has the opposite sign to that of previous instant and has the magnitude decreased within the time available for demagnetization. The second figure shows the applied external torque, adding the perturbation of the gravity gradient with the control torque generated by the magnetic actuators. It is interesting to note that the curve follows the magnetization and demagnetization cycle, since the magnitude of the control torque has the same order of magnitude of gravity gradient that is 10^{-8}.

Extending iteration time to 1000 s and not including limit zone control, the angular velocity module is diminished like presented in Figure 9. The B-dot control is able to detumble the spacecraft. However, as illustrated in Figure 10, the angle

δ oscillates and satellite enter forbidden zone for 339 s, or 33.9% of the simulated time. As angular velocity is large, there is no problem because it stays in such orientation for a small period. However, as rotation is decreased, it is possible that spacecraft continue pointing to Earth for a long time. Thus, limit zone control is incorporated.

Table 1 – Satellite Simulation Parameters.

Parameters	Value	Parameter	Value
Eccentricity	0.01	Initial roll angle, ψ	45°
Semimajor axis	8378137 m	Initial pitch angle, θ	10°
Ascending node	300°	Initial yaw angle, ϕ	30°
Perigee argument	45°	Initial angular velocity, $\boldsymbol{\omega}_{\mathbf{B}}^{\mathbf{BO}}$	$[0.04 \;\; 0.04 \;\; 0.04]^T$ rad/s
Inclination	85°	Maximum dipole moment, m_{max}	0.4 A.m^2
Initial mean anomaly	0°	B-dot control gain, k_m	1.098×10^{-5} kg.m^2/s
Orbital rate, ω_s	8.233×10^{-4} rad/s	Growth parameter, k_g	2 s
Sample time sensors, ΔT	1 s	Damping parameter, ξ	0.1358
Sample time actuators, Δt	0.01 s	Damped oscillator frequency, ω_n	22.08 rad/s
J_x	8.333×10^{-3} kg.m^2	Limit zone angle criteria, δ_e	10°
J_y	8.333×10^{-3} kg.m^2	Iteration period	1000 s
J_z	3.333×10^{-3} kg.m^2	Initial date	01/01/2023 at 00:00 UT

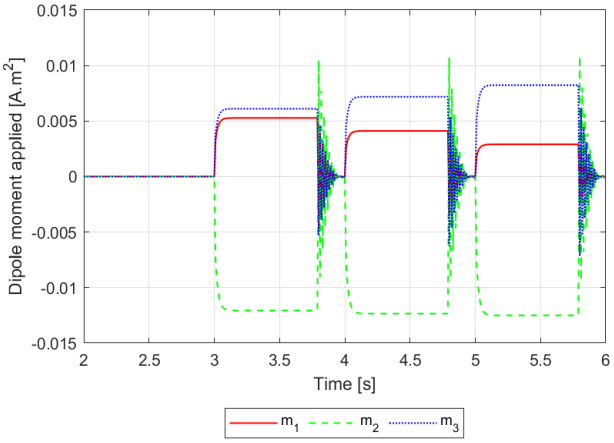

Figure 7. Dipole moment applied in slowdown mode illustrating magnetization and demagnetizing cycle.

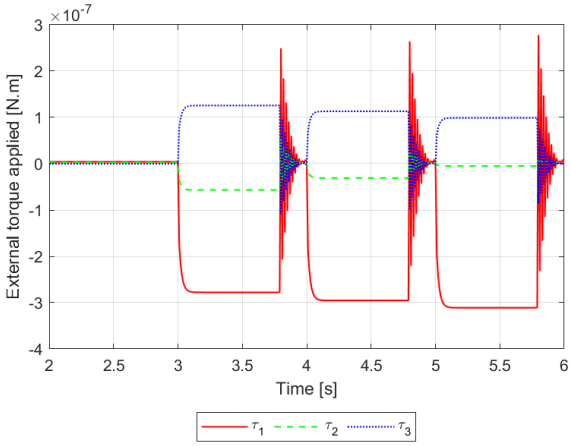

Figure 8. External torque applied in slowdown mode illustrating magnetization and demagnetizing cycle.

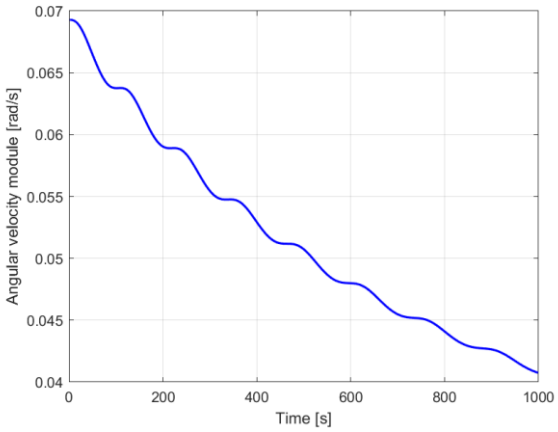

Figure 9. Angular velocity module $\left\|\boldsymbol{\omega}_{\mathbf{B}}^{\mathbf{BO}}\right\|$ in time without limit zone control.

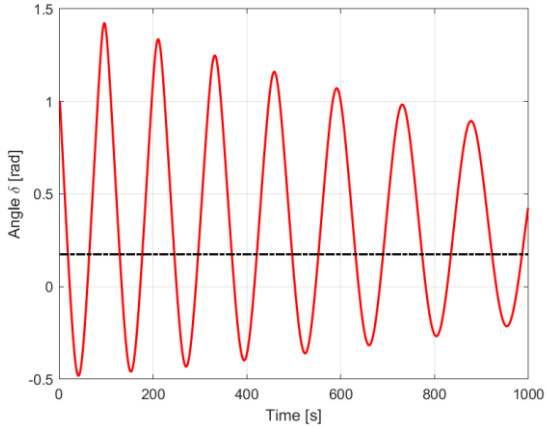

Figure 10. Angle δ in red and angle criteria $\delta_e = 0.1745$ rad in dash-dotted black without limit zone control.

Applying limit control zone with criteria $\delta \leq \delta_e$ we can see that the control works because after 300 s of simulation, as can be seen in Figure 11, the satellite no longer enters the prohibited zone, however the consequences for this to occur are seen in Figure 12. The angular velocity module behaves in a non-linear way, always leading to an increase in

magnitude, even exceeding the value of 5°/s. Since the limit zone mode is applied for a long time (a total time of 271 s), speed is largely increased so that the slowdown mode is not able to decrease in the time that it is operative. Presented in Figure 13, there are at least three modes during simulations: slowdown mode, shown as 3-valued line, limit zone mode, shown as 2-valued line and detumbling, shown as 1-valued line. Limit zone mode is activated nine times. We can conclude that limit zone mode is able to take the satellite's cone of sight out of the boundary zone at the expense of increasing body rotation.

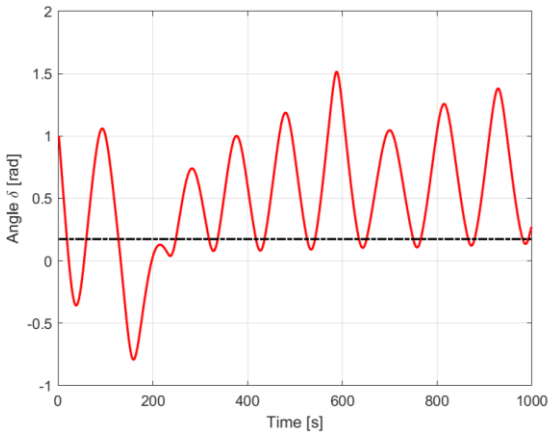

Figure 11. Angle δ with limit zone control type 1.

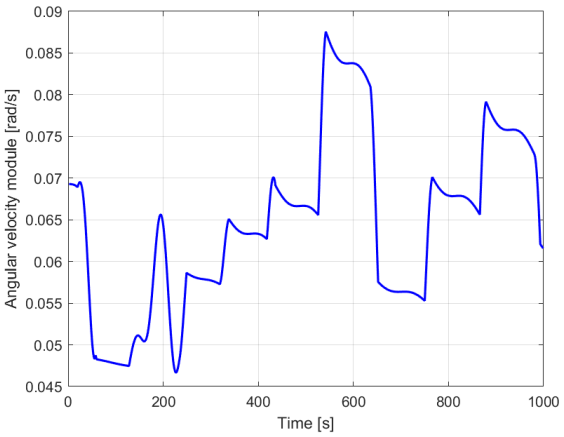

Figure 12. Angular velocity module $\|\boldsymbol{\omega}_{\mathbf{B}}^{\mathbf{BO}}\|$ in time with control type 1.

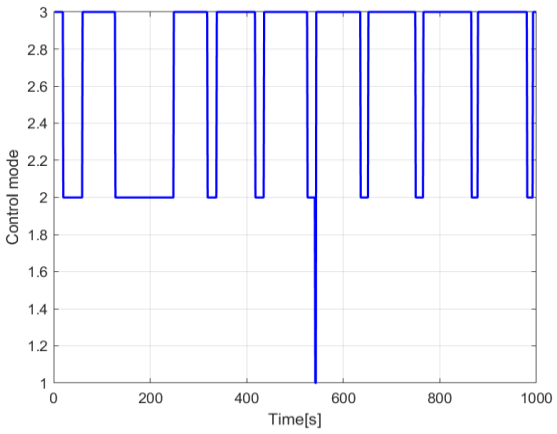

Figure 13. Variations of control mode type 1.

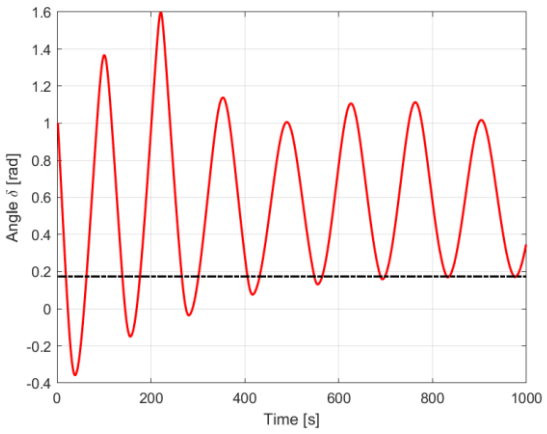

Figure 14. Angle δ with limit zone control type 2.

. As a solution to the amount of time spent in mode 2, a new methodology is presented including a new criterion, analysis of $\Delta\delta \leq 0$, expressed as

$$\Delta\delta = \delta_k - \delta_{k-1} \tag{25}$$

Now type 1 is named control limit zone just with analyzing δ and type 2 is named the control analyzing δ and $\Delta\delta$. The performance of δ in type 2 is presented in Figure 14. In this case, activation of limit zone control only occurs in the direction of decreasing δ, thus, the exit from the limit zone occurs at lower speeds. The amount of time in limit zone is 72 s, representing 7.2% of total simulation and analyzing the behavior of the δ-curve, after 300 s the system does not tend to pass the δ_e. The limit zone control is activated for 81 s, which is less than type 1 and analyzing Figure 15, it can be said that the angular velocity has a more stable behavior, as the slowdown mode can perform the proper deceleration for a longer time. In Figure 16 we present the variation in control methodologies as satellite tends to enter limit zone. Comparing this figure to Figure 13, energy is saved, and the boundary zone mode can be limited to a short activation given the low rotation speed.

Table 2 summarizes the performance between the analyzed control types. The second column presents the time spent with the satellite's cone of sight within the limit zone. In the third column we have the time spent in activating the limit

zone control. The type with the best performance is type 3 whose activation of the limit zone control occurs through the verification of $\delta \leq \delta_e$ and $\Delta\delta \leq 0$, due to the shorter time exposed to the limit zone (72 s) and the shorter time activating the control to exit it (81 s).

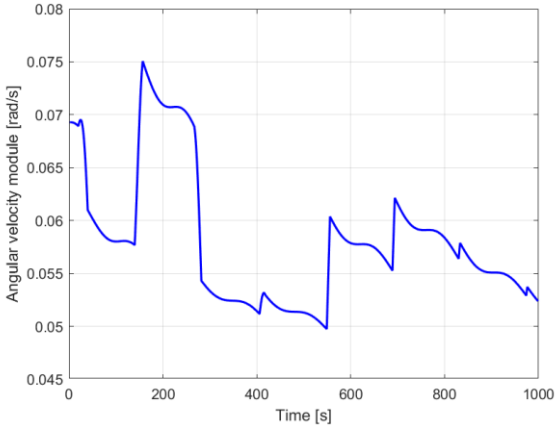

Figure 15. Angular velocity module $\|\boldsymbol{\omega}_{\mathbf{B}}^{\mathbf{BO}}\|$ in time with control type 2.

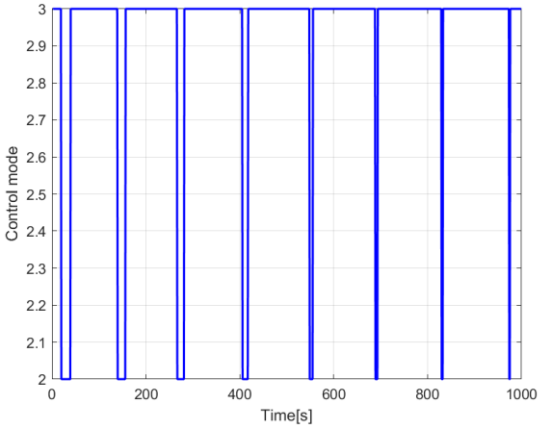

Figure 16. Variations of control mode type 2.

Table 2. Performance of control methodologies in relation to time in the limit zone and duration of actuation.

Strategy	Time $\delta < 0$ [s]	Limit control zone duration [s]
No control	339	0
Type 1	97	271
Type 2	72	81

5. CONCLUSION

This work presents the problem of designing the attitude control of the NANOMIRAX/CRON-1 satellite, in which it is required that its camera avoids the pointing towards the Earth. Three control modes are considered: 1) Detumbling mode, 2) Limit zone mode and 3) Slowdown mode. Detumbling should be a major priority when the speed is higher than 5°/s. Below this value, the slowdown mode is the methodology considered to reduce spacecraft's rotation, however it should not be the priority.

For low speeds the limit zone mode should be activated to avoid spacecraft's cone of sight to capture the Earth surface. This mode can perform this task, providing the highest dipole moment available from the magnetic actuators. However, the higher the angular velocity of the satellite when activating the control, the longer it takes to exit it. The best criterion is to analyze the separation angle between body and orbital frame and its variation on time.

Another analyzed behavior was the magnetization and demagnetizing cycle present in ferromagnetic actuators. The magnetization can be modeled as an exponential function, while the demagnetization cycle is modeled as a damped harmonic oscillator.

Future steps of this work include the improvement in the attitude actuation possibilities with the combination of reaction wheels and magnetorquer rods and other attitude control modes like some stable pointing tasks to interest targets to more detailed data collection about some gamma- and x-rays bursts.

6. ACKNOWLEDGEMENTS

The authors wish to acknowledge the financial support from the Brazilian National Research Council (CNPq, Brazil), through a MSc. Scholarship, in the context of the MAI-DAI program (UFABC, Brazil).

7. REFERENCES

Alken, P., Thébault, E., Beggan, C.D. and al., e. (2021) 'International Geomagnetic Reference Field: the thirteenth generation', *Earth, Planets and Space*, vol. 73, no. 49, pp. 1-25.

Avanzini, G. and Giulietti, F. (2012) 'Magnetic Detumbling of a Rigid Spacecraft', *Journal of Guidance, Control, and Dynamics*, vol. 135, no. 4, pp. 1326-1334.

Berland, G.D., Marshall, R.A., Martin, C., Mhadgut, D., Buescher, J., Kohnert, R.A., Boyajian, S., Cully, C.M. and McCarthy, M.P. (2021) 'The AEPEX CubeSat Mission: Quantifying Energetic Particle Precipitation through Bremsstrahlung X-Ray Imaging', 35th Annual Small Satellite Conference, Virtual Version, 1-14.

Bertotti, G. (1998) *Hysteresis in Magnetism*, San Diego: Academic Press.

Braga, J., D'Amico, F., Avila, M.A.C., Penacchioni, A.V., Sacahui, J.R., Jr., V.A.d.S., Mattiello-Francisco, F., Strauss, C. and Fialho, M.A.A. (2015) 'The protoMIRAX hard X-Ray imaging balloon experiment', *Astronomy & Astrophysics*, pp. 1-9.

Braga, J., Durão, O.S.C., Castro, M., D'Amico, F., Stecchini, P.E., Amirábile, S., Blanco, F.G., Strauss, C., Silva, W., Schad, V.R. and Reitano, L.A. (2020) 'LECX: A cubesat experiment to detect and localize cosmic explosions in hard X-rays', *Royal Astronomical Society*, vol. 493, February, pp. 4852-4860.

Braga, J., Rothschild, R., Heise, J., Staubert, R., Remillard, R., D'Amico, F., Jablonski, F., Heindl, W., Matteson, J., Kuulkers, E., Wilms, J. and Kendziorra, E. (2004) 'MIRAX: a Brazilian X-Ray astronomy satellite mission', *Advances in Space Research*, pp. 2657-2661.

Cheng, Y. and Shuster, M.D. (2014) 'Improvement to the Implementation of the QUEST Algorithm', *Journal of Guidance, Control, and Dynamics*, vol. 37, no. 1, pp. 301-305.

Coey, J.M.C. (2010) *Magnetism and Magnetic Materials*, Cambridge: Cambridge University Press.

Crassidis, J.L. and Junkins, J.L. (2012) *Optimal Estimation of Dynamic Systems*, Boca Raton: CRC Press.

Cullity, B.D. and Graham, C.D. (2009) *Introduction to Magnetic Materials*, 2nd edition, Hoboken: John Willey & Sons.

Desouky, M.A.A. and Abdelkhalik, O. (2019) 'Improved Magnetic Attitude Control', 2019 IEEE National Aerospace and Electronics Conference, Dayton, 552-559.

Durão, O.S.C., Braga, J., Schad, V.R., Neto, M.B.d.S., Esper, M., Rigobello, G. and Ribeiro, C.B. (2019) 'CRON-1 The First Brazilian Private Cubesat', 33rd Annual AIAA/USU Conference on Small Satellites, Utah.

Lovera, M. (2015) 'Magnetic satellite detumbling: the b-dot algorithm revisited', 2015 American Control Conference, Chicago, 1867-1872.

Markley, F.L. and Crassidis, J.L. (2014) *Fundamentals of Spacecraft Attitude Determination and Control*, New York: Springer.

Ninomiya, K., Uo, M., Maeda, K. and Saitoh, T. (1990) 'Attitude Control System of the X-Ray Observatory Astro-D', 11th Triennial World Congress, Tallinn, 99-106.

Ogata, K. (2010) *Modern Control Engineering*, 5th edition, New Jersey: Prentice Hall.

Pirayesh, R., Naseri, A., Stochaj, S., Shah, N. and Krizmanic, J. (2018) 'Attitude Control optimization of a Virtual Telescope for X-ray observations', 32nd Annual AIAA/USU Conference of Small Satellites, Utah, 1-13.

Shuster, M.D. and Natanson, G.A. (1993) 'Quaternion Computation from a Geometric Point of View', *The Journal of the Astronautical Sciences*, October-December, pp. 545-556.

Shuster, M.D. and Oh, S.D. (1981) 'Three-Axis Attitude Determination from Vector Observations', *Journal of Guidance and Control*, vol. 4, no. 1, pp. 70-77.

Thornton, S.T. and Marrion, J.B. (2004) *Classical Dynamics of Particle and Systems*, 5th edition, Belmont: Brooks/Cole.

Vallado, D.A. (2013) *Fundamentals of Astrodynamics and Applications*, 4th edition, Hawthorne: Springer.

Viegas, W.d.V.C. and Waldmann, J. (2010) 'Aquisição Inicial e Estabilização de Atitude em 3 eixos de um Satélite Universitário de Baixo Custo por um Viés em Roda de Momentum e Controle Magnético', VI Congresso Nacional de Engenharia Mecânica, Campina Grande.

Wertz, J. (ed.) (1978) *Spacecraft Attitude Determination and Control*, Dordrecht: Kluwer Academic Publishers.

Zheng, T., Cheng, F., Rui, X. and Ji, X. (2019) 'A Precise Algorithm for Computing Sun Position on a Satellite', *Journal of Aerospace Technology*, pp. 1-12.

8. RESPONSIBILITY NOTICE

The authors are the only responsible for the printed material included in this paper.